ACS APPLIED MATERIALS & INTERFACES

Research Article

www.acsami.org

Fe_3O_4@$NiFe_xO_y$ Nanoparticles with Enhanced Electrocatalytic Properties for Oxygen Evolution in Carbonate Electrolyte

Zhishan Luo,[†] Sara Martí Sànchez,[‡] Raquel Nafria,[†] Gihan Joshua,[†] Maria de la Mata,[‡] Pablo Guardia,[†,§] Cristina Flox,[†] Carlos Martínez-Boubeta,[⊥] Konstantinos Simeonidis,[∥] Jordi Llorca,[#] Joan Ramon Morante,[†] Jordi Arbiol,[‡,⊗] Maria Ibáñez,[†] and Andreu Cabot*[,†,⊗]

[†]Catalonia Institute for Energy Research - IREC, Sant Adrià de Besòs, Barcelona 08930, Spain

[‡]Catalan Institute of Nanoscience and Nanotechnology (ICN2), CSIC and The Barcelona Institute of Science and Technology (BIST), Campus UAB, Bellaterra, 08193 Barcelona, Spain

[§]Centre de Tecnologia Química de Catalunya and Universitat Rovira i Virgili, Carrer de Marcel·lí Domingo s/n, 43007 Tarragona, Spain

[⊥]Freelancer, Santiago de Compostela 15701, Spain

[∥]Department of Physics, Aristotle University Thessaloniki, 54124 Thessaloniki, Greece

[#]Institut de Tècniques Energètiques, Universitat Politècnica de Catalunya, 08028 Barcelona, Spain

[⊗]ICREA, Pg. Lluís Companys 23, 08010 Barcelona, Spain

Supporting Information

ABSTRACT: The design and engineering of earth-abundant catalysts that are both cost-effective and highly active for water splitting are crucial challenges in a number of energy conversion and storage technologies. In this direction, herein we report the synthesis of Fe_3O_4@$NiFe_xO_y$ core−shell nanoheterostructures and the characterization of their electrocatalytic performance toward the oxygen evolution reaction (OER). Such nanoparticles (NPs) were produced by a two-step synthesis procedure involving the colloidal synthesis of Fe_3O_4 nanocubes with a defective shell and the posterior diffusion of nickel cations within this defective shell. Fe_3O_4@$NiFe_xO_y$ NPs were subsequently spin-coated over ITO-covered glass and their electrocatalytic activity toward water oxidation in carbonate electrolyte was characterized. Fe_3O_4@$NiFe_xO_y$ catalysts reached current densities above 1 mA/cm^2 with a 410 mV overpotential and Tafel slopes of 48 mV/dec, which is among the best electrocatalytic performances reported in carbonate electrolyte.

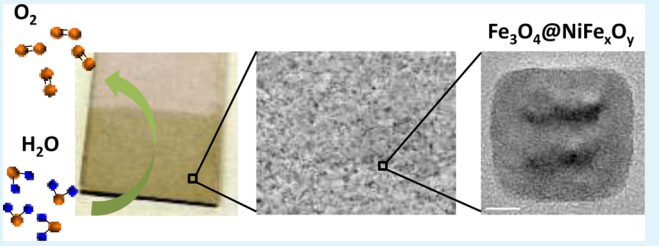

KEYWORDS: *nanoparticle, iron oxide, magnetite, core−shell nanostructure, electrocatalysts, oxygen evolution reaction, OER*

1. INTRODUCTION

The electrocatalytic OER has a key and limiting role in several energy conversion and storage technologies, such as metal-air batteries, fuel cells, and electrolyzers.[1−3] A main challenge of water oxidation is its slow kinetics associated with a multistep proton-coupled electron transfer process that involves four protons and four electrons ($4OH^- \rightarrow 2H_2O + O_2 + 4e^-$, in basic media). OER generally requires voltages significantly above the thermodynamic potential for water splitting, which has an efficiency cost. To reduce this potential, OER catalysts based on expensive and scarce noble metals, such as IrO_2 and RuO_2,[4−6] are currently used, which have an economic cost that limits the penetration of related technologies in huge markets, such as transportation and grid integration of renewable energies. Consequently, an enormous interest exists in developing stable OER catalysts that are able to lower the kinetic barriers associated with the OER and at the same time are based on earth-abundant metals.

Over the years, a plethora of compounds have been explored as OER catalysts.[7−19] A good catalyst must have (i) small energy steps between the involved chemical and charge transfer steps, to minimize overall overpotential; (ii) a proper strength of the bond between metal cations and oxygen/hydroxide species;[5,7,8] (iii) high surface areas with proper porosity to maximize the density of accessible reaction sites per electrode unit area; (iv) large density of proper reaction sites, which may call for defective structures with low energy of formation of proper defects and even amorphous materials;[9,10] (v) high electrical conductivities to maximize current densities, especially in thick porous layers providing large number of sites per electrode area unit; (vi) proper catalyst-electrode energy band alignment preventing Schottky barriers in the

Received: August 7, 2016
Accepted: October 12, 2016

DOI: 10.1021/acsami.6b09888
ACS Appl. Mater. Interfaces XXXX, XXX, XXX−XXX

common case of using semiconductor catalysts; and (vii) high stability at operation conditions.

A number of transition metal compounds have exhibited particularly attractive activities and durabilities for water oxidation in alkaline electrolytes. Among them Ni−Fe oxides, hydroxides, or oxyhydroxides at reaction conditions are the most promising earth-abundant OER catalysts under alkaline conditions.[9,20−33] Within these materials, Ni is generally considered the active oxygen evolution center.[8,31] On the other hand, Fe incorporation provides improved electrical conductivities,[20,34] partial charge transfer modifying Ni site energy,[20,33] stabilization of proper crystal phases and/or proper Ni oxidation states, and also an increased strain, defect density, and overall lower crystallinity.[21] Some authors have also proposed iron cations within the Ni−Fe oxide structure as the active sites with near optimal adsorption energies for the intermediates formed during the OER.[11] In this regard the iron chemical state is also modified by the Ni environment and even Fe^{4+} species, which may be the active species when in corners, edges or defect sites, were identified under OER conditions in Ni−Fe catalysts using Mössbauer spectroscopy.[22]

The pH has a particularly strong influence in Ni−Fe oxide/oxyhydroxide catalysts, which was attributed to a deprotonation of Ni-based catalysts to form active oxygen species that may act as the OER precursor.[23] OER metal oxide catalysts are operated at high pH values to maximize activity. However, the use of pH values closer to neutral has advantages, such as an improved stability of the cell components and improved safety during processing and use.[35−38] As an example, Cao and co-workers reported a Fe-based film as highly active electrocatalysts in neutral aqueous solution.[36] Besides, Zaharieva et al. demonstrated an excellent performance of electrodeposited Mn oxide catalysts for electrochemical water oxidation at neutral pH solution.[37] CO_2-saturated carbonate solutions are increasingly used as relatively low pH electrolyte with the additional potential of multifunctionality as water splitting can be combined with CO_2 reduction to produce carbon-based liquid fuels. Another potential advantage is that carbonate solutions are also more environmental friendly than for instance the phosphate buffer which may cause critical eutrophication of water body.[39,40] Considerable effort has been devoted to the development of transition metal oxides as OER catalysts in carbonate electrolyte.[41−43] As an example, Sun et al. reported a Fe-based electrocatalyst in carbonate electrolyte having a 560 mV overpotential at 10 mA/cm^2 and 34 mV/dec of Tafel slope.[19] Joya and co-workers demonstrated that Ni-based electrocatalysts in a bicarbonate electrolyte reached a slope of −63 mV/pH, close to the theoretical value of −59 mV/pH for a PCET mechanism involving one electron and one proton.[44]

In terms of processing, most electrocatalysts are currently coated as powders onto conductive substrates with the aid of polymeric binders, such as Nafion.[45] The use of a binder can decrease liquid−solid interface and reduce electrical conductivity of the electrode, while at the same time it can have associated stability problems due to peel off. Over flat substrates, electrodeposition and vacuum-based thin film techniques generally yield compact crystalline layers, with low specific surfaces and thus activities. Instead the use of mesostructured supports, such as stainless steel meshes or nickel foams, provides much higher areas and activities.[24,46] Alternatively, the printing or deposition of colloidal NPs with tuned compositions not only potentially provides highly porous layers, but also an unmatched composition control at the nanometer scale using high-throughput and high yield chemical routes at ambient pressure and low temperature.[47−51] The huge potential of such solution-based strategies to tune material properties at the nanoscale resides in the ability to chemically manipulate material growth from the very initial combination of atoms into a cluster, and to do so in parallel for huge amounts of NPs, all self-evolving at the same rate and in the same conditions. Thus, very large amounts of material in the form of colloidal NPs with precisely tuned properties can be produced in a simple, fast, and cost-effective manner. Colloidal synthesis routes are also extremely versatile, allowing production of elemental or multinary nanoparticles with a wide range of compositions and also multimaterial nanoheterostructures with organized phase distribution by the parallel or sequential growth of one material at the surface of the other or by replacing part of the ions of a preformed nanostructure.[52−55]

Herein, we report the colloidal synthesis of a novel Fe−Ni oxide OER catalyst based on core−shell NPs containing a Fe_3O_4 core and a $NiFe_xO_y$ shell. Such Fe_3O_4@$NiFe_xOy$ core−shell NPs were produced by a simple and scalable protocol involving the diffusion of nickel cations within the defective shell of Fe_3O_4 NPs. This simple strategy yielded a catalyst ink that was easily applicable to any support using low cost solution-processing technologies and without the use of polymeric binders. We further demonstrate the suitability of the synthesized materials and used processes to produce OER catalysts in a carbonate electrolyte that are beyond the state-of-the-art in terms of activity and stability.

2. EXPERIMENTAL SECTION

Chemicals. Cobalt(II) perchlorate hexahydrate ($Co(ClO_4)_2\cdot 6H_2O$), nickel(II) perchlorate hexahydrate ($Ni(ClO_4)_2\cdot 6H_2O$), sodium oleate (Na-OA, ≥ 82%), octadecene (ODE, 90%) xylenes (≥98.5%), oleylamine (OLA, > 70%), and oleic acid (OA, 90%) were purchased from Sigma-Aldrich. Toluene, hexane, chloroform, acetone, and ethanol were of analytical grade and obtained from various sources. Milli-Q water was supplied by the PURELAB flex from ELGA. All chemicals were used as received without further purification, except OLA, which was purified by distillation.

Synthesis Fe_3O_4 Nanocubes. Fe_3O_4 nanocubes were used as a template for the synthesis of Fe_3O_4@$NiFe_xO_y$ core−shell NPs. Several routes can be found in the literature to produce such nanostructures. We followed and detail here a procedure developed from merging two previously reported protocols.[56,57] First, iron oleate (Fe-OA) was obtained by dissolving 1.3 g (8 mmol) of $FeCl_3$ and 7.3 g (24 mmol) of sodium oleate (Na-OA) in a mixture of 12 mL H_2O, 16 mL ethanol, and 28 mL hexane. The resulting mixture was stirred overnight at room temperature and purified in a separatory funnel by washing 5−6 times with preheated (80 °C) MQ-water (18.2 MΩ, filtered with filter pore size 0.22 μM, Millipore). The resulting organic layer was dried under reduced pressure in a rotary evaporator until all remaining H_2O was removed. Once purified, 0.4 g of Fe-OA (4.44 mmol), 0.1 g of Na-OA (3.28 mmol), 0.1 mL of OA (0.32 mmol), and 10 mL of ODE were mixed in a 25 mL three-neck flask and degassed under magnetic stirring for 1.5 h at 70 °C (0.2−0.3 mbar). The reaction mixture was then heated to 330 °C (5.5 °C/min) under an argon blanket and kept at that temperature for 30 min. The solution was then cooled down to room temperature and NPs were collected by adding 20 mL of acetone and centrifuging at 9000 rpm for 10 min. The black/brown precipitate was redispersed in 5 mL of chloroform under sonication and washed at least 2 times more. Finally the NPs were dispersed and stored in 5 mL of chloroform. Within this synthesis protocol, variation of the OA concentration, heating ramp, and reflux temperature would allow for size tuning.

Synthesis of Fe_3O_4@$NiFe_xO_y$ NPs. In a 25 mL three-neck flask, 10 mg of Fe_3O_4 NPs, weighed after precipitation and drying, were

DOI: 10.1021/acsami.6b09888
ACS Appl. Mater. Interfaces XXXX, XXX, XXX−XXX

dissolved in 5 mL of xylene along with 0.41 mL of OLA (1.26 mmol) and 0.08 mL (0.26 mmol) of OA and heated to 90 °C. Then, 0.5 mL of $Ni(ClO)_2{\cdot}6H_2O$ aqueous solution (0.2 M) was injected into the reaction solution under vigorous stirring and kept at 90 °C in air for 5 h. Finally, the solution was cooled down to room temperature and NPs were collected by adding 15 mL of ethanol. The precipitate was redispersed in 5 mL of toluene and precipitated again with ethanol. Finally NPs were resuspended in 5 mL of toluene for further characterization.

Structural, Chemical, and Magnetic Characterization. Transmission electron microscopy (TEM) analyses were carried out using a ZEISS LIBRA 120, operating at 120 kV. High-resolution TEM (HRTEM) and scanning TEM (STEM) studies were conducted using a field emission gun FEI Tecnai F20 microscope at 200 kV with a point-to-point resolution of 0.19 nm. High angle annular dark-field (HAADF) STEM was combined with electron energy loss spectroscopy (EELS) in the Tecnai F20, by using a GATAN QUANTUM filter. Samples were prepared by drop casting a solution of NPs on a 200 mesh copper grid. Scanning electron microscopy (SEM) analyses were performed using a ZEISS Auriga microscope with an energy dispersive X-ray spectroscopy (EDS) detector operating at 20 kV, that allowed for analysis of the NP composition. For SEM characterization, the materials were dispersed in chloroform and drop casted onto silicon substrates. Powder X-ray diffraction (XRD) patterns were collected directly from the as-synthesized NPs dropped on Si(501) substrate on a Bruker AXS D8 Advance X-ray diffractometer with Ni-filtered (2 μm thickness) Cu K radiation (λ = 1.5406 Å) operating at 40 kV and 40 mA. A LynxEye linear position-sensitive detector was used in reflection geometry. X-ray photoelectron spectroscopy (XPS) was done on a SPECS system equipped with an Al anode XR50 source operating at 150 mW and a Phoibos 150 MCD-9 detector. The pressure in the analysis chamber was always below 10−7 Pa. The area analyzed was about 2 mm × 2 mm. The pass energy of the hemispherical analyzer was set at 25 eV and the energy step was set at 0.1 eV. Data processing was performed with the CasaXPS program (Casa Software Ltd., UK). Binding energy (BE) values were centered using the C 1s peak at 284.8 eV. The atomic fractions (%) were calculated using peak areas. Magnetic hysteresis loops of the powder material were recorded at room temperature using an Oxford Instruments 1.2 H/CF/HT vibrating sample magnetometer (VSM) with a maximum applied field of 1 T. Magnetizations were corrected for the organic content of the materials (20−30%) as measured by thermogravimetry.

Electrolytes and Catalyst Preparation. The carbonate buffer solution was prepared by mixing equal volume of 0.2 M Na_2CO_3 and 0.2 M $NaHCO_3$ aqueous solutions.[19] The pH was monitored by using a pH meter. To prepare the catalysts films, Fe_3O_4 and Fe_3O_4@$NiFe_xO_y$ NPs were dispersed in octane with a concentration of about 10 mg/mL. ITO glass substrates were coated with the NPs by spin-coating. Briefly, 200 μL of the suspension was gradually dropped at 200 rpm. After the substrate was spun for 1 min, the speed was increased up to 900 rpm and kept at this speed for 1 additional minute. To make different NPs layers, the iron-based films were dried on a hot-plate (~110 °C) to completely evaporate the solvent and then the spin-coating process was repeated. The obtained films were denoted ITO-Fe_3O_4 for Fe_3O_4 NPs and ITO-Fe_3O_4−Ni# for Fe_3O_4@$NiFe_xO_y$ NPs, where # is the number of layers deposited by the spin-coating process (# = 1−4). Then these films were annealed for 30 min at 300 °C in 5% H_2/Ar atmosphere.

Electrochemical Characterization. Electrochemical measurements were carried out on a computer-controlled workstation bipotentiostat (Versa STAT 3, Princeton Applied Research). The custom-made three-electrode system that was used included 25 mL of carbonate electrolyte with a pH of 9.75, a silver−silver chloride reference electrode (Ag/AgCl with saturated KCl encapsulated, 012167 RE-1B, ALS Co. Ltd.-BAS Inc.), a platinum foil for the counter electrode, and a 1.5 cm^2 ITO glass with or without catalysts for the working electrode. A scan rate of 50 mV/s was used for all the current density measurements. All potentials are reported versus the reversible hydrogen electrode (RHE) using the Nernst equation as follows:

$$E_{RHE} = E_{Ag/AgCl} + 0.059\times pH + E^{o}_{Ag/AgCl}(V) \quad (1)$$

where pH is the electrolyte pH and $E^{o}_{Ag/AgCl}$ = 0.197 V versus the normal hydrogen electrode (NHE) at 25 °C for the Ag/AgCl/saturated KCl solution (CH Instruments, Inc.). The OER overpotential (η) was calculated using the equation below:

$$\eta = E_{Ag/Ag} - E^{o}(O_2/H_2O)(V) \quad (2)$$

where E^{o} (O_2/H_2O) is the thermodynamic potential for water oxidation (the OER) relative to Ag/AgCl at pH = 9.75, which was calculated to be 0.65 V using,

$$E^{o}(O_2/H_2O) = 1.23 - 0.059\times pH - E^{o}_{Ag/AgCl}(V) \quad (3)$$

All the potentials reported here were *iR*-corrected. Current densities were calculated using geometric surface areas.

O_2 Evolution Evaluation. We used gas chromatography to analyze the reaction products and calculate the Faradaic efficiency for O_2 production. For this measurement, the electrochemical reaction was carried out within a gastight electrochemical cell containing a silver−silver chloride reference electrode (Ag/AgCl with saturated KCl encapsulated), a glass fritted isolated platinum counter-electrode, and a 1.5 cm^2 ITO-Fe_3O_4−Ni anodized catalysts as the working electrode. Before measurement, the electrochemical cell was purged by bubbling Ar for 2 h. The experiment was carried out at 1.3 V vs RHE in 80 mL carbonate buffer solution. The produced oxygen was extracted using a 18 mL/min Ar flow introduced using a mass flow controller. The gaseous outlet flow from the cell was analyzed online every 10 min using a two channel gas microchromatograph (490 Micro GC) equipped with an M5A 20 m and a PPQ 10 m columns and TCD detectors. The steam water was condensed before the gas chromatography analyses using a trap kept at 175 K. The Faradaic efficiency was calculated by measuring the amount of oxygen in the effluent gas, taking into account the Ar gas flow and comparing these values with the charge transferred calculated from the current density measured with the potentiostat. Figure S1 shows a photograph of the experimental setup used for this measurement.

Figure 1 shows a scheme of the synthetic protocol used to prepare the Fe−Ni oxide NPs and the process used to produce the NP-based electrocatalyst.

3. RESULTS AND DISCUSSION

Figure 2 shows representative TEM images, size distribution histograms, and XRD patterns of the initial iron oxide NPs and the final iron−nickel oxide NPs produced following the above

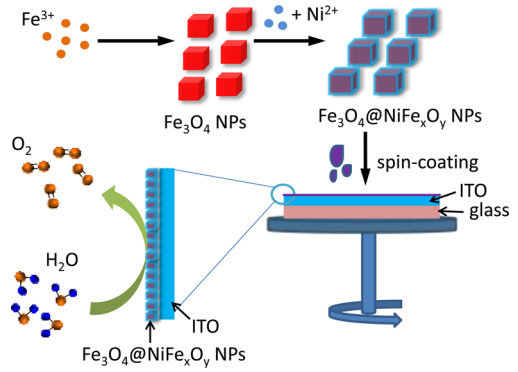

Figure 1. Scheme of the synthesis of core−shell Fe_3O_4@$NiFe_xO_y$ NPs as a result of the growth of a shell on top of Fe_3O_4 seeds. Thin films were fabricated by spin coating a solution of NPs on top of an ITO substrate and their electrocatalytic performance in water oxidation was tested.

DOI: 10.1021/acsami.6b09888
ACS Appl. Mater. Interfaces XXXX, XXX, XXX−XXX

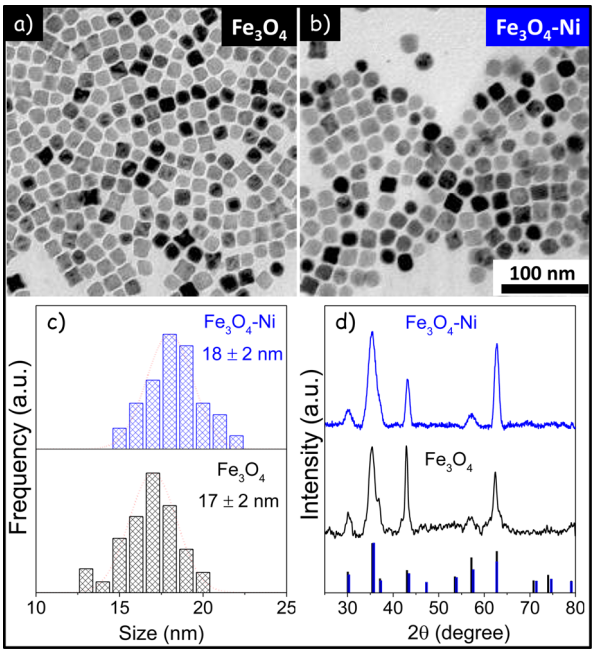

Figure 2. Representative TEM micrograph of Fe_3O_4 NPs (a) and Fe_3O_4−Ni NPs (b). Their corresponding size distribution histograms (c) and XRD patterns (d), including reference patterns for Fe_3O_4 (black bars, JCPDS 00-001-1111) and $Ni_{0.6}Fe_{2.4}O_4$ (blue bars, JCPDS 01-087-2338).

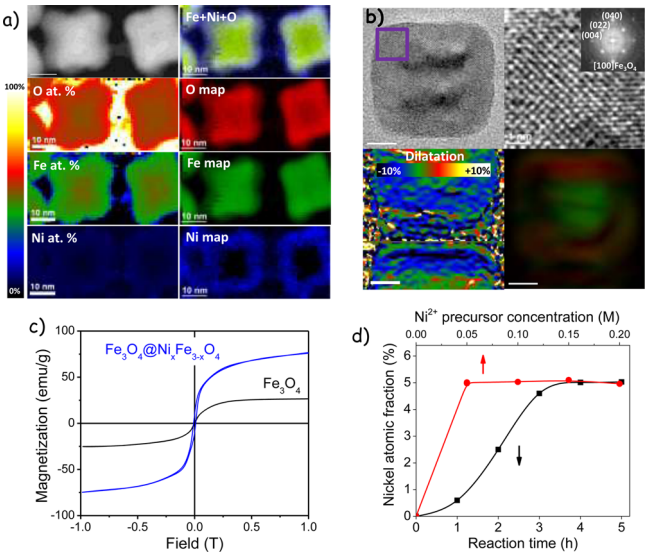

Figure 3. (a) Low magnification ADF STEM image, relative atomic composition, and elemental maps of Ni, Fe, and O; (b) HRTEM micrographs of Fe_3O_4@$NiFe_xO_y$, detail of the squared region and their corresponding indexed power spectrum (inset), HRTEM shows Moiré contrasts, dilatation map applying GPA to the (040) planes of Fe_3O_4@$NiFe_xO_y$ core−shell NPs, and structural map obtained with the (040) plane revealing differences in *d*-spacing between core and shell; (c) Magnetization hysteresis loops of Fe_3O_4 and Fe_3O_4@$NiFe_xO_y$ NPs; (d) EDX data showing the molar fraction of Ni as a function of the molarity of the precursor solution of Ni^{2+} added during the synthesis (red line, 0.5 mL injected, reaction time = 5 h) and as a function of the reaction time increasing (black line, 0.5 mL injected of a 0.2 M Ni^{2+} precursor solution).

detailed procedure. The NP's morphology did not change with the introduction of nickel ions and the average size just very slightly increased from 17 ± 2 nm to 18 ± 2 nm (Figure 2c). XRD patterns (Figure 2d) revealed the initial iron oxide NPs and the final iron- nickel oxide NPs to have a cubic inverse spinel structure, as it corresponds to magnetite Fe_3O_4 and the maghemite γ-Fe_2O_3 defective structure. Following previous reports, we indexed it as magnetite (JCPDS 01-086-1350).[56,57] The peak broadening due to the small crystal domain size and the very similar unit cell parameters of Fe_3O_4 and iron−nickel oxides with an inverse spinel structure, such as $Ni_{0.6}Fe_{2.4}O_4$ (JCPDS 01-087-2338), prevented an explicit identification of any effect of Ni on the NP's crystal phase from the XRD pattern. Using Scherrer's equation, we calculated the size of Fe3O4 and iron−nickel oxide NPs to be 17 and 20 nm respectively, in good agreement with TEM results.

ICP analysis revealed the overall [Ni]/[Fe] ratio of the NP ensemble to be [Ni]/[Fe] = 0.1. SEM-EDX analyses at different points of the sample confirmed this elemental ratio and demonstrated excellent compositional homogeneity at the micrometer scale. To determine the elemental distribution within each NP, low magnification annular dark field (ADF) STEM and chemical maps were further acquired (Figure 3a). Elemental compositional maps, obtained by EELS using O K, Fe $L_{2,3}$, and Ni $L_{2,3}$ edges, revealed the presence of Fe and O throughout all the cubic-shaped NPs, but with a 3% increase in oxygen content and 6% reduction in Fe atomic percent at the outer parts of the NP with respect to the center. On the other hand, Ni was only detected at the outer parts of the NPs (Figure 3a), reaching almost 5% of the total composition there.

Figure S2 and Figure 3b show representative HRTEM micrograph of Fe_3O_4 and Fe_3O_4@$NiFe_xO_y$ NPs, respectively, and details of their crystal structure. The power spectrum of the HRTEM of Fe_3O_4@$NiFe_xO_y$ (Figure 3b) could be fitted with that of magnetite (space group FD3-MZ) with a = b = c = 8.4082 Å. Both the core and the shell showed the same cubic Space Group: FD3-MZ. The dark contrasts that can be observed in the micrographs might correspond to Moiré fringes caused by two lattices with a small mismatch. Geometrical phase analysis (GPA) analyses also showed a decrease in the $d_{(040)}$-spacing on the outer parts of the NP (Figure 3b). From these results, we calculated differences of cell spacing between the core and the shell of around 4%, which cannot be explained by just taking into account the Ni diffusion. Notice that the difference in lattice parameter between Fe_3O_4 and $NiFe_2O_4$ structures should be about 1%, and that the amount of Ni in the shell of the NPs here produced was even lower: [Ni]/[Fe] ∼ 0.12. Besides, similar contrasts were also observed on the original iron oxide NPs (Figure 2a). Checking for the relative composition of the oxygen in Figure 3a it is clearly observed that the shell is more oxidized than the core. Thus, we hypothesize that original NPs already have a core−shell structure with a magnetite core and a more oxidized, defective maghemite shell. This hypothesis explains the difference in lattice constant and the contrasts observed in the low magnification TEM image on Fe_3O_4 and Fe_3O_4@$NiFe_xO_y$ NPs.

To support this hypothesis, we measured the magnetic properties of the produced NPs, magnetization being a property particularly sensitive to crystallinity. As observed in Figure 3c, Fe_3O_4 NPs were characterized by relatively low magnetization values compared with bulk magnetite, which clearly points toward the presence of a defective surface structure. Surprisingly, the addition of Ni significantly increased magnetization, in opposition to what is expected taking into

DOI: 10.1021/acsami.6b09888
ACS Appl. Mater. Interfaces XXXX, XXX, XXX−XXX

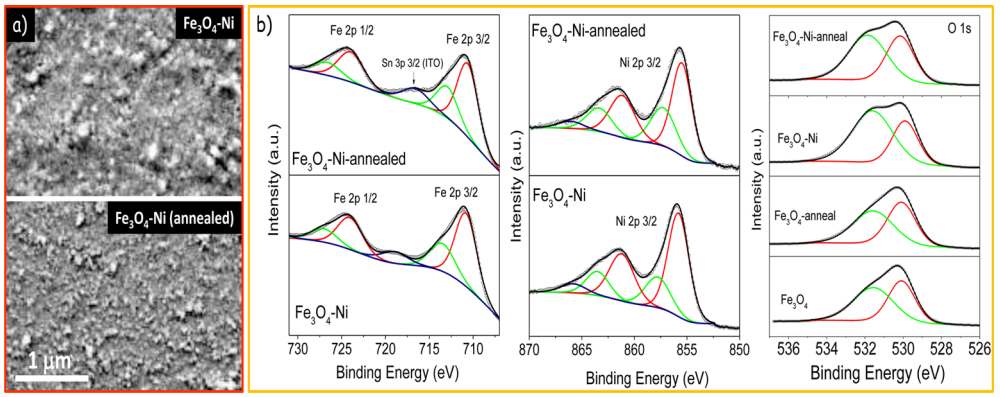

Figure 4. (a) SEM micrographs of Fe_3O_4@$NiFe_xO_y$ catalyst film before and after annealing. (b) Fe 2p, Ni 2p, and O 1s regions of the XPS spectra of the catalyst layers before and after annealing.

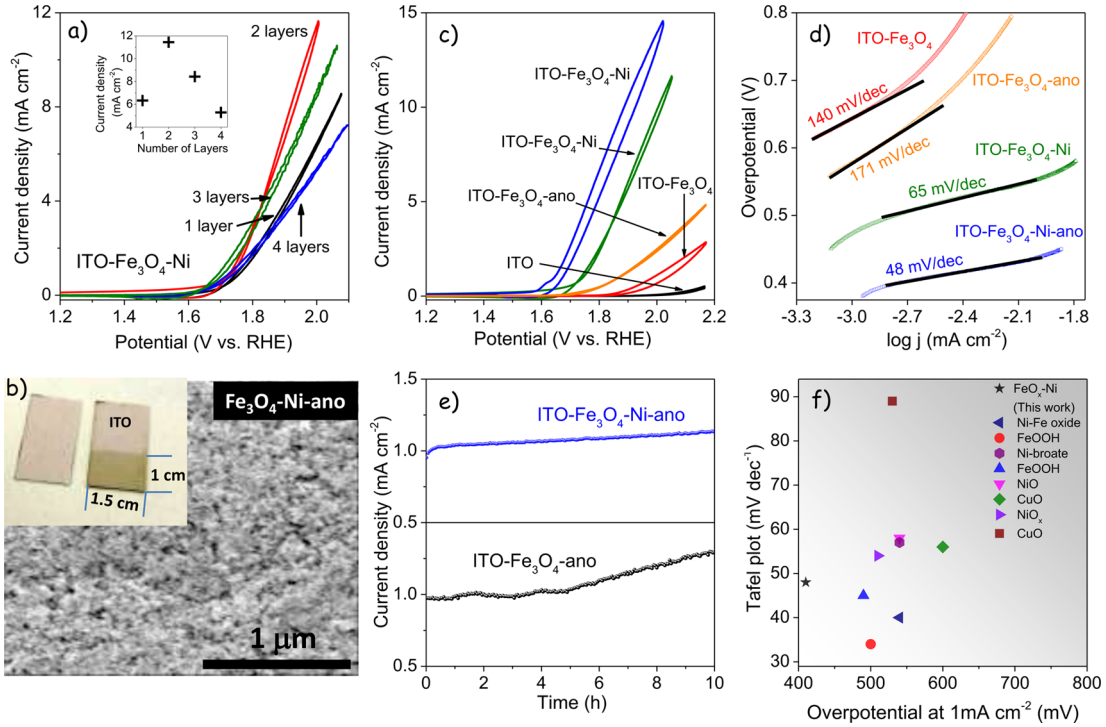

Figure 5. (a) CV of ITO-Fe_3O_4−Ni catalysts with different film thicknesses. (b) Photograph (inset) of ITO glass (left) and ITO-Fe_3O_4−Ni catalyst film after anodization (right) and SEM image of the ITO-Fe_3O_4−Ni catalysts after the anodization process. (c) CV of ITO and the different catalysts. (d) Corresponding Tafel plot of the different catalyst. (e) Stability measurements of ITO-Fe_3O_4-ano and ITO-Fe_3O_4−Ni-ano catalyst films. (f) Comparison of overpotential at 1 mA/cm^2 and Tafel slopes between transition metal-based OER catalysts reported at neutral or near neutral pH condition.[19,21,59−64] Conditions: 0.2 M pH 9.75 carbonate buffer electrolyte, RE is Ag/AgCl, CE is Pt foil, scan rate 50 mV/s, electrode area 1.5 cm^2.

account the lower saturation magnetization of nickel ferrite when compared to that of magnetite. We believe that such an increase of the saturation might be associated with the partial reconstruction of the magnetically frustrated layer on the surface of the Fe_3O_4 seeds due directly to the Ni incorporation or to the additional annealing of the NPs at temperatures close to 100 °C during the Ni diffusion.

From these results, we further hypothesize that the defective shell helps Ni incorporation to the lattice and that this Ni incorporation is limited to the defective shell structure. We observe that the Ni diffusion is self-limited in terms of localization (Figure 3a) and concentration. In this last direction, the amount of Ni in the final core−shell NPs gradually increased with the reaction time up to 4 h and remained stable after this mark (Figure 3d). The concentration of Ni in the core−shell NPs was kept almost the same even when increasing amounts of nickel precursor were introduced (Figure 3d). These experimental evidence and the low nickel ratio obtained even at relatively high nickel precursor concentrations and after long reaction times point toward a self-limited diffusion of Ni within the Fe_3O_4 structure.

The use of a perchlorate precursor was critical to incorporate nickel within the iron oxide and to produce NPs with a core−shell compositional distribution. When following the exact same procedure but using a chloride ($NiCl_2$) instead of a perchlorate precursor, Ni was not detected within the NPs. Differences may be ascribed to the lower coordination ability of perchlorate rather than chloride ions, which make perchlorate precursors slightly more reactive and thus inclined to the cation incorporation within the Fe_3O_4 structure than chloride

DOI: 10.1021/acsami.6b09888
ACS Appl. Mater. Interfaces XXXX, XXX, XXX−XXX

precursors.[52] The reaction of the nickel perchlorate precursor in the absence of Fe_3O_4 seeds resulted in the formation of $Ni(OH)_2$ nanosheets (Figure S3).

To study Fe_3O_4 and Fe_3O_4@$NiFe_xO_y$ core−shell NPs toward OER, NPs were spin coated onto ITO-coated glass substrates (Figure 1). The layer thickness could be controlled by the number of spin coating steps or the concentration of the deposited NP solution. SEM micrographs of the ITO-Fe_3O_4 and ITO-Fe_3O_4−Ni films revealed the catalyst to have a relatively rough surface (Figure 4a). After deposition, the catalysts were annealed under 5% H_2/Ar atmosphere at 300 °C for 30 min. This annealing process did not significantly change the composition or distribution of the chemical states of the films according to XPS analysis (Figure 4b); the surface atomic [Ni]/[Fe] ratio changed slightly from 0.62 to 0.55 after annealing and a slight negative shift, ∼ 0.3 eV, of the Ni $2P_{3/2}$ binding energy was obtained with the annealing process in a hydrogen atmosphere. XPS further demonstrated the presence of at least two types of oxygen at the NP surface. The component at lower binding energies (529.9−530.1 eV) corresponds to lattice oxygen in metal oxide and the component at higher binding energies (531.6−531.8 eV) to hydroxide groups at the surface. Significantly higher contributions of the hydroxide groups at the surface of the Ni-containing sample were observed.

The OER catalytic activity of the as-prepared catalyst films were evaluated by cyclic voltammetry (CV) using a carbonate buffer solution as electrolyte (pH = 9.75). To optimize the catalyst thickness, the ITO-Fe_3O_4−Ni performance was initially analyzed as a function of the number of layers deposited. Catalyst films that were too thin provided a reduced number of sites for the water oxidation reaction, resulting in relatively low current densities. On the other hand, catalyst films that were rather thick had associated lower performances due to an increase of the electrical resistivity. We found the optimum thickness to be around 60 nm, which corresponded to two spin coating processes (Figure 5a,b).

Setting a constant potential above the water oxidation onset, we observed that the current density increases over time (Figure S4). This beneficial anodization process has been previously used to electrochemically activate the catalyst. For example, Nocera and co-workers reported that the anodization process led to changes of the oxidation state and the structure of electrodeposited Ni-based catalyst films, resulting in markedly improved catalytic activity.[58] Sun et al. also demonstrated that after anodization, electrodeposited FeOOH catalysts exhibited lower overpotential and Tafel slope and higher current density compared with nonanodized films.[19] However, I. Roger and M.D. Symes demonstrated the incorporation of small amounts of impurities, such as Ni, during anodization processes could result in strong increase of current densities.[59] Our catalytic films were not produced by electrodeposition but by the spin coating of previously formed nanocrystals, which have a relatively high chemical and structural stability. Furthermore, we found similar relative anodization effects in catalysts with different surface compositions, but final current densities for the different anodized catalysts were quite different, discarding a main electrocatalytic effect of an incorporated impurity. Minor crystallographic and/or chemical modification of the NCs may take place during anodization (although no evidence in this direction could be obtained) and these could have an effect on the electrocatalytic performance. However, we hypothesize the main anodization effect on our materials could be associated with the removal by oxidation of residual organic species and possibly carbon from the NCs surface freeing surface sites for electrochemical reaction. Actually, SEM analysis shows the electrodes after anodization to present more clearly defined NCs, denoting a lower contamination (Figure S5).

Figure 5c shows CV characterization of ITO-Fe_3O_4 and ITO-Fe_3O_4−Ni, before and after anodization. The CV profile of ITO is also plotted as a reference although it exhibited almost no catalytic activity. Generally, the as-anodized catalyst films showed superior OER activities compared to nonanodized films. In particular, ITO-Fe_3O_4−Ni-ano displayed a much lower overpotential (η = 410 mV at 1 mA·cm^{-2}) than ITO-Fe_3O_4−Ni (η = 520 mV), ITO-Fe_3O_4 (η = 750 mV), and ITO-Fe_3O_4-ano (η = 640 mV). The corresponding Tafel slopes are shown in Figure 5d. ITO-Fe_3O_4−Ni-ano also showed the lowest Tafel slopes, down to 48 mV/dec, as compared to ITO-Fe_3O_4−Ni (65 mV/dec), ITO-Fe_3O_4 (140 mV/dec), and ITO-Fe_3O_4-ano (171 mV/dec). The catalyst stability at a current density of 1 mA·cm^{-2} in carbonate electrolyte was also evaluated. As shown in Figure 5e, the anodized catalysts displayed no decrease of activity with time, but a slight increase of current density was obtained. Overall, such ITO-Fe_3O_4−Ni-ano catalyst films were superior to most transition metal-based OER catalysts at near neutral pH conditions previously reported (Figure 5f and Table 1).

Table 1. Comparisons of Different Earth-Abundant Transition Metal Water Oxidation Catalysts at pH 9−9.75

catalyst	overpotential at 1 mA cm^{-2} (mV)	Tafel slope (mV dec^{-1})	pH	reference
FeO_x-Ni	410	48	9.75	this work
FeOOH	500	34	9.75	19
Ni−Fe Oxide	540	40	9.2	21
Nickel-broate	540	57	9.2	59
FeOOH	490	45	9.2	60
NiO	540	58	9.2	61
CuO	600	56	9.2	62
NiO_x	510	54	9.2	63
CuO	530	89	9.0	64
IrO_x·nH_2O	200 (1.5 mA cm^{-2})	52	9.0	65

We used the ITO-Fe_3O_4−Ni anodized catalysts operated at 1.3 V vs RHE to measure the Faradaic efficiency for O_2 production. At this potential, the working electrode provided a current of 4.5 ± 0.1 mA (Figure S8), which corresponds to around 2.8 ± 0.6 x10^{16} e/s and would translate to the production of 7.0 ± 0.2 × 10^{15} O_2/s. The gaseous reaction products were extracted using a 18 ± 1 mL/min Ar flow, which in the stationary state and considering a 100% O_2 production yield would translate into an oxygen concentration of a 0.095 ± 0.06%. After calibrating our gas chromatograph to measure oxygen concentrations in this range, we measured an oxygen concentration on the effluent gas of 0.096 ± 0.008% (Figure S8). Thus, a Faradaic efficiency of 101 ± 8% was calculated.

The same strategies were applied to incorporate cobalt and manganese ions into Fe_3O_4 NPs using cobalt and manganese perchlorates as cation precursors, and catalysts were fabricated with the obtained NPs. In Figure 6, the electrocatalytic

DOI: 10.1021/acsami.6b09888
ACS Appl. Mater. Interfaces XXXX, XXX, XXX−XXX

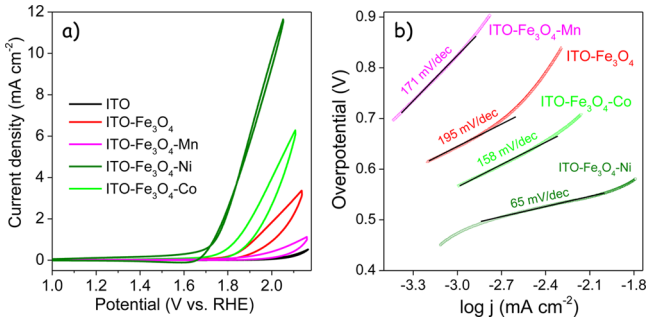

Figure 6. (a) CV of ITO and different catalysts. (b) Corresponding Tafel plot of the different catalyst. Conditions: 0.2 M pH 9.75 carbonate buffer electrolyte, RE is Ag/AgCl, CE is Pt foil, scan rate 50 mV/s, electrode area 1.5 cm^2.

properties of the obtained compounds are plotted. The ITO-Fe_3O_4−Co catalyst film exhibited higher OER activity than ITO-Fe_3O_4 catalyst, with an overpotential η = 620 mV at 1 mA·cm^{-2}, and a corresponding Tafel slope of 158 mV/dec However, the ITO-Fe_3O_4−Mn catalyst film showed a lower OER activity compared with all other catalysts tested, indicating the incorporation of Mn to reduce the Fe_3O_4 performance toward water oxidation.

4. CONCLUSION

In summary, Fe_3O_4@$NiFe_xO_y$ core−shell NPs were synthesized at low temperature and in air atmosphere by a two-step method involving Ni cation diffusion within the outer defective shell of Fe_3O_4 template NPs. Such core−shell NPs were deposited onto ITO glass by a spin-coating process to form thin catalyst films, which exhibited high electrocatalytic activity for OER in carbonate electrolyte. In particular, the as-anodized core−shell catalyst film showed low overpotenital of 410 mV at 1 mA/cm^2 and Tafel slope of 48 mV/dec This core−shell NP synthetic protocol can be expanded as a general strategy to grow metal oxide heterostructures for OER or for other applications. Furthermore, the magnetic properties of the NPs could be improved during the shell growth process, providing potentially useful materials for environmental remediation, purification, and biomedical applications, among others.

■ ASSOCIATED CONTENT

Supporting Information

The Supporting Information is available free of charge on the ACS Publications website at DOI: 10.1021/acsami.6b09888.

Additional experimental details and structural, chemical, and functional characterization results (PDF)

■ AUTHOR INFORMATION

Corresponding Author

*acabot@irec.cat.

Notes

The authors declare no competing financial interest.

■ ACKNOWLEDGMENTS

This work was supported by the European Regional Development Funds and the Spanish MINECO project BOOSTER, TNT-FUELS, e-TNT, Severo Ochoa Excellence Program, and PEC−CO2. Z.L. thanks the China Scholarship Council for scholarship support. P.G. acknowledges the People Programme (Marie Curie Actions) of the FP7/2007-2013 European Union Program (TECNIOspring grant agreement no. 600388) and the Agency for Business Competitiveness of the Government of Catalonia, ACCIÓ. M.I. thanks AGAUR for Beatriu de Pinós postdoctoral grant (2013 BP-A00344). J.L. is Serra Húnter Fellow and is grateful to ICREA Academia program. S.M.S. acknowledges funding from "Programa Internacional de Becas "la Caixa"-Severo Ochoa". Authors also acknowledge the funding from Generalitat de Catalunya 2014 SGR 1638.

■ REFERENCES

(1) Jiao, Y.; Zheng, Y.; Jaroniec, M.; Qiao, S. Z. Design of Electrocatalysts for Oxygen- and Hydrogen-involving Energy Conversion Reactions. *Chem. Soc. Rev.* **2015**, *44*, 2060−2086.

(2) Chen, D.; Chen, C.; Baiyee, Z. M.; Shao, Z.; Ciucci, F. Nonstoichiometric Oxides as Low-Cost and Highly-Efficient Oxygen Reduction/Evolution Catalysts for Low-Temperature Electrochemical Devices. *Chem. Rev.* **2015**, *115*, 9869−9921.

(3) Neburchilov, V.; Wang, H.; Martin, J. J.; Qu, W. A Review on Air Cathodes for Zinc−air Fuel Cells. *J. Power Sources* **2010**, *195*, 1271−1291.

(4) Trasatti, S. Electrocatalysis by Oxides-Attempt at A Unifying Approach. *J. Electroanal. Chem. Interfacial Electrochem.* **1980**, *111*, 125−131.

(5) Reier, T.; Oezaslan, M.; Strasser, P. Electrocatalytic Oxygen Evolution Reaction (OER) on Ru, Ir, and Pt Catalysts: A Comparative Study of Nanoparticles and Bulk Materials. *ACS Catal.* **2012**, *2*, 1765−1772.

(6) McCrory, C. C. L.; Jung, S.; Peters, J. C.; Jaramillo, T. F. Benchmarking Heterogeneous Electrocatalysts for the Oxygen Evolution Reaction. *J. Am. Chem. Soc.* **2013**, *135*, 16977−16987.

(7) Burke, M. S.; Enman, L. J.; Batchellor, A. S.; Zou, S.; Boettcher, S. W. Oxygen Evolution Reaction Electrocatalysis on Transition Metal Oxides and (Oxy)hydroxides: Activity Trends and Design Principles. *Chem. Mater.* **2015**, *27*, 7549−7558.

(8) Trotochaud, L.; Ranney, J. K.; Williams, K. N.; Boettcher, S. W. Solution-Cast Metal Oxide Thin Film Electrocatalysts for Oxygen Evolution. *J. Am. Chem. Soc.* **2012**, *134*, 17253−17261.

(9) Smith, R. D. L.; Prévot, M. S.; Fagan, R. D.; Zhang, Z.; Sedach, P. A.; Siu, M. K. J.; Trudel, S.; Berlinguette, C. P. Photochemical Route for Accessing Amorphous Metal Oxide Materials for Water Oxidation Catalysis. *Science* **2013**, *340*, 60−63.

(10) Bockris, J. O.; Otagawa, T. Mechanism of Oxygen Evolution on Perovskites. *J. Phys. Chem.* **1983**, *87*, 2960−2971.

(11) Friebel, D.; Louie, M. W.; Bajdich, M.; Sanwald, K. E.; Cai, Y.; Wise, A. M.; Cheng, M.-J.; Sokaras, D.; Weng, T.-C.; Alonso-Mori, R.; Davis, R. C.; Bargar, J. R.; Nørskov, J. K.; Nilsson, A.; Bell, A. T. Identification of Highly Active Fe Sites in (Ni,Fe)OOH for Electrocatalytic Water Splitting. *J. Am. Chem. Soc.* **2015**, *137*, 1305−1313.

(12) Gong, M.; Zhou, W.; Tsai, M.-C.; Zhou, J.; Guan, M.; Lin, M.-C.; Zhang, B.; Hu, Y.; Wang, D.-Y.; Yang, J.; Pennycook, S. J.; Hwang, B.-J.; Dai, H. Nanoscale Nickel Oxide/Nickel Heterostructures for Active Hydrogen Evolution Electrocatalysis. *Nat. Commun.* **2014**, *5*, 4695.

(13) Cheng, Y.; Jiang, S. P. Advances in Electrocatalysts for Oxygen Evolution Reaction of Water Electrolysis - from Metal Oxides to Carbon Nanotubes. *Prog. Nat. Sci.* **2015**, *25*, 545−553.

(14) Galán-Mascarós, J. R. Water Oxidation at Electrodes Modified with Earth-Abundant Transition-Metal Catalysts. *ChemElectroChem* **2015**, *2*, 37−50.

(15) Smith, R. D. L.; Prévot, M. S.; Fagan, R. D.; Trudel, S.; Berlinguette, C. P. Water Oxidation Catalysis: Electrocatalytic Response to Metal Stoichiometry in Amorphous Metal Oxide Films Containing Iron, Cobalt, and Nickel. *J. Am. Chem. Soc.* **2013**, *135*, 11580−11586.

DOI: 10.1021/acsami.6b09888
ACS Appl. Mater. Interfaces XXXX, XXX, XXX−XXX

(16) Menezes, P. W.; Indra, A.; Levy, O.; Kailasam, K.; Gutkin, V.; Pfrommer, J.; Driess, M. Using Nickel Manganese Oxide Catalysts for Efficient Water Oxidation. *Chem. Commun.* **2015**, *51*, 5005−5008.
(17) Roger, I.; Symes, M. D. First Row Transition Metal Catalysts for Solar-driven Water Oxidation Produced by Electrodeposition. *J. Mater. Chem. A* **2016**, *4*, 6724−6741.
(18) Fabbri, E.; Habereder, A.; Waltar, K.; Kötz, R.; Schmidt, T. Developments and Perspectives of Oxide-based Catalysts for The Oxygen Evolution Reaction. *Catal. Sci. Technol.* **2014**, *4*, 3800−3821.
(19) Li, F.; Bai, L.; Li, H.; Wang, Y.; Yu, F.; Sun, L. An Iron-based Thin Film as A Highly Efficient Catalyst for Electrochemical Water Oxidation in A Carbonate Electrolyte. *Chem. Commun.* **2016**, *52*, 5753−5756.
(20) Trotochaud, L.; Young, S. L.; Ranney, J. K.; Boettcher, S. W. Nickel−Iron Oxyhydroxide Oxygen-Evolution Electrocatalysts: The Role of Intentional and Incidental Iron Incorporation. *J. Am. Chem. Soc.* **2014**, *136*, 6744−6753.
(21) Louie, M. W.; Bell, A. T. An Investigation of Thin-Film Ni−Fe Oxide Catalysts for the Electrochemical Evolution of Oxygen. *J. Am. Chem. Soc.* **2013**, *135*, 12329−12337.
(22) Chen, J. Y. C.; Dang, L.; Liang, H.; Bi, W.; Gerken, J. B.; Jin, S.; Alp, E. E.; Stahl, S. S. Operando Analysis of NiFe and Fe Oxyhydroxide Electrocatalysts for Water Oxidation: Detection of Fe^{4+} by Mössbauer Spectroscopy. *J. Am. Chem. Soc.* **2015**, *137*, 15090−15093.
(23) Trześniewski, B. J.; Diaz-Morales, O.; Vermaas, D. A.; Longo, A.; Bras, W.; Koper, M. T. M.; Smith, W. A. In Situ Observation of Active Oxygen Species in Fe-Containing Ni-Based Oxygen Evolution Catalysts: The Effect of pH on Electrochemical Activity. *J. Am. Chem. Soc.* **2015**, *137*, 15112−15121.
(24) Lu, X.; Zhao, C. Electrodeposition of Hierarchically Structured Three-Dimensional Nickel−Iron Electrodes for Efficient Oxygen Evolution at High Current Densities. *Nat. Commun.* **2015**, *6*, 6616.
(25) Hoang, T. T. H.; Gewirth, A. A. High Activity Oxygen Evolution Reaction Catalysts from Additive-Controlled Electrodeposited Ni and NiFe Films. *ACS Catal.* **2016**, *6*, 1159−1164.
(26) Chen, H.; Huang, X.; Zhou, L.-J.; Li, G.-D.; Fan, M.; Zou, X. Electrospinning Synthesis of Bimetallic Nickel−Iron Oxide/Carbon Composite Nanofibers for Efficient Water Oxidation Electrocatalysis. *ChemCatChem* **2016**, *8*, 992−1000.
(27) Görlin, M.; Chernev, P.; Ferreira de Araújo, J.; Reier, T.; Dresp, S.; Paul, B.; Krähnert, R.; Dau, H.; Strasser, P. Oxygen Evolution Reaction Dynamics, Faradaic Charge Efficiency, and the Active Metal Redox States of Ni−Fe Oxide Water Splitting Electrocatalysts. *J. Am. Chem. Soc.* **2016**, *138*, 5603−5614.
(28) Qi, J.; Zhang, W.; Xiang, R.; Liu, K.; Wang, H.-Y.; Chen, M.; Han, Y.; Cao, R. Porous Nickel−Iron Oxide as a Highly Efficient Electrocatalyst for Oxygen Evolution Reaction. *Adv. Sci.* **2015**, *2*, 1500199.
(29) Ali-Löytty, H.; Louie, M. W.; Singh, M. R.; Li, L.; Sanchez Casalongue, H. G.; Ogasawara, H.; Crumlin, E. J.; Liu, Z.; Bell, A. T.; Nilsson, A.; Friebel, D. Ambient-Pressure XPS Study of a Ni−Fe Electrocatalyst for the Oxygen Evolution Reaction. *J. Phys. Chem. C* **2016**, *120*, 2247−2253.
(30) Long, X.; Li, J.; Xiao, S.; Yan, K.; Wang, Z.; Chen, H.; Yang, S. A Strongly Coupled Graphene and FeNi Double Hydroxide Hybrid as an Excellent Electrocatalyst for the Oxygen Evolution Reaction. *Angew. Chem., Int. Ed.* **2014**, *53*, 7584−7588.
(31) Zhang, W.; Qi, J.; Liu, K.; Cao, R. A Nickel-Based Integrated Electrode from an Autologous Growth Strategy for Highly Efficient Water Oxidation. *Adv. Energy Mater.* **2016**, *6*, 1502489.
(32) Song, F.; Hu, X. Exfoliation of Layered Double Hydroxides for Enhanced Oxygen Evolution Catalysis. *Nat. Commun.* **2014**, *5*, 4477.
(33) Gong, M.; Li, Y.; Wang, H.; Liang, Y.; Wu, J. Z.; Zhou, J.; Wang, J.; Regier, T.; Wei, F.; Dai, H. An Advanced Ni−Fe Layered Double Hydroxide Electrocatalyst for Water Oxidation. *J. Am. Chem. Soc.* **2013**, *135*, 8452−8455.
(34) Corrigan, D. A. The Catalysis of The Oxygen Evolution Reaction by Iron Impurities in Thin Film Nickel Oxide Electrodes. *J. Electrochem. Soc.* **1987**, *134*, 377−384.
(35) Wu, Y.; Chen, M.; Han, Y.; Luo, H.; Su, X.; Zhang, M.-T.; Lin, X.; Sun, J.; Wang, L.; Deng, L.; Zhang, W.; Cao, R. Fast and Simple Preparation of Iron-Based Thin Films as Highly Efficient Water-Oxidation Catalysts in Neutral Aqueous Solution. *Angew. Chem., Int. Ed.* **2015**, *54*, 4870−4875.
(36) Chen, M.; Wu, Y.; Han, Y.; Lin, X.; Sun, J.; Zhang, W.; Cao, R. An Iron-based Film for Highly Efficient Electrocatalytic Oxygen Evolution from Neutral Aqueous Solution. *ACS Appl. Mater. Interfaces* **2015**, *7*, 21852−21859.
(37) Zaharieva, I.; Chernev, P.; Risch, M.; Klingan, K.; Kohlhoff, M.; Fischer, A.; Dau, H. Electrosynthesis, Functional, and Structural Characterization of A Water-oxidizing Manganese Oxide. *Energy Environ. Sci.* **2012**, *5*, 7081−7089.
(38) Kanan, M. W.; Nocera, D. G. In Situ Formation of an Oxygen-Evolving Catalyst in Neutral Water Containing Phosphate and Co^{2+}. *Science* **2008**, *321*, 1072−1075.
(39) Paytan, A.; McLaughlin, K. The Oceanic Phosphorus Cycle. *Chem. Rev.* **2007**, *107*, 563−576.
(40) Diaz, J.; Ingall, E.; Benitez-Nelson, C.; Paterson, D.; de Jonge, M. D.; McNulty, I.; Brandes, J. A. Marine Polyphosphate: A Key Player in Geologic Phosphorus Sequestration. *Science* **2008**, *320*, 652−655.
(41) Kim, J. H.; Magesh, G.; Kang, H. J.; Banu, M.; Kim, J. H.; Lee, J.; Lee, J. S. Carbonate-coordinated Cobalt Co-catalyzed $BiVO_4/WO_3$ Composite Photoanode Tailored for CO_2 Reduction to Fuels. *Nano Energy* **2015**, *15*, 153−163.
(42) Surendranath, Y.; Dincă, M.; Nocera, D. G. Electrolyte-Dependent Electrosynthesis and Activity of Cobalt-Based Water Oxidation Catalysts. *J. Am. Chem. Soc.* **2009**, *131*, 2615−2620.
(43) Chen, Z.; Kang, P.; Zhang, M.-T.; Stoner, B. R.; Meyer, T. J. Cu(ii)/Cu(0) Electrocatalyzed CO_2 and H_2O Splitting. *Energy Environ. Sci.* **2013**, *6*, 813−817.
(44) Joya, K. S.; Takanabe, K.; de Groot, H. J. M. Surface Generation of a Cobalt-Derived Water Oxidation Electrocatalyst Developed in a Neutral HCO_3^-/CO_2 System. *Adv. Energy Mater.* **2014**, *4*, 1400252.
(45) Herranz, T.; Ibáñez, M.; Gómez de la Fuente, J. L.; Pérez-Alonso, F. J.; Peña, M. A.; Cabot, A.; Rojas, S. In Situ Study of Ethanol Electrooxidation on Monodispersed Pt3Sn Nanoparticles. *ChemElectroChem* **2014**, *1*, 885−895.
(46) Perez-Alonso, F.; Adan, C.; Rojas, S.; Pena, M.; Fierro, J. Ni/Fe Electrodes Prepared by Electrodeposition Method over Different Substrates for Oxygen Evolution Reaction in Alkaline Medium. *Int. J. Hydrogen Energy* **2014**, *39*, 5204−5212.
(47) Ibáñez, M.; Cabot, A. All Change for Nanocrystals. *Science* **2013**, *340*, 935−936.
(48) Nafria, R.; Genç, A.; Ibáñez, M.; Arbiol, J.; Ramírez de la Piscina, P.; Homs, N.; Cabot, A. Co−Cu Nanoparticles: Synthesis by Galvanic Replacement and Phase Rearrangement during Catalytic Activation. *Langmuir* **2016**, *32*, 2267−2276.
(49) Luo, Z.; Ibáñez, M.; Antolín, A. M.; Genç, A.; Shavel, A.; Contreras, S.; Medina, F.; Arbiol, J.; Cabot, A. Size and Aspect Ratio Control of Pd_2Sn Nanorods and Their Water Denitration Properties. *Langmuir* **2015**, *31*, 3952−3957.
(50) Zamani, R. R.; Ibáñez, M.; Luysberg, M.; García-Castelló, N.; Houben, L.; Prades, J. D.; Grillo, V.; Dunin-Borkowski, R. E.; Morante, J. R.; Cabot, A.; Arbiol, J. Polarity-Driven Polytypic Branching in Cu-Based Quaternary Chalcogenide Nanostructures. *ACS Nano* **2014**, *8*, 2290−2301.
(51) Ibáñez, M.; Luo, Z.; Genc, A.; Piveteau, L.; Ortega, S.; Cadavid, D.; Dobrozhan, O.; Liu, Y.; Nachtegaal, M.; Zebarjadi, M.; Arbiol, J.; Kovalenko, M. V.; Cabot, A. High-Performance Thermoelectric Nanocomposites from Nanocrystal Building Blocks. *Nat. Commun.* **2016**, *7*, 10766.
(52) Luo, Z.; Irtem, E.; Ibáñez, M.; Nafria, R.; Marti-Sanchez, S.; Genç, A.; de la Mata, M.; Liu, Y.; Cadavid, D.; Llorca, J.; Arbiol, J.; Andreu, T.; Morante, J. R.; Cabot, A. Mn_3O_4@$CoMn_2O_4$-Co_xO_y Nanoparticles: Partial Cation Exchange Synthesis and Electrocatalytic

DOI: 10.1021/acsami.6b09888
ACS Appl. Mater. Interfaces XXXX, XXX, XXX−XXX

739 Properties toward the Oxygen Reduction and Evolution Reactions.
740 *ACS Appl. Mater. Interfaces* **2016**, *8*, 17435−17444.
741 (53) Yu, X.; Liu, J.; Genç, A.; Ibáñez, M.; Luo, Z.; Shavel, A.; Arbiol,
742 J.; Zhang, G.; Zhang, Y.; Cabot, A. Cu_2ZnSnS_4−Ag_2S Nanoscale p−n
743 Heterostructures as Sensitizers for Photoelectrochemical Water
744 Splitting. *Langmuir* **2015**, *31*, 10555−10561.
745 (54) Yu, X.; Shavel, A.; An, X.; Luo, Z.; Ibáñez, M.; Cabot, A.
746 Cu_2ZnSnS_4-Pt and Cu_2ZnSnS_4-Au Heterostructured Nanoparticles for
747 Photocatalytic Water Splitting and Pollutant Degradation. *J. Am. Chem.*
748 *Soc.* **2014**, *136*, 9236−9239.
749 (55) Yu, X.; An, X.; Genç, A.; Ibáñez, M.; Arbiol, J.; Zhang, Y.; Cabot,
750 A. Cu_2ZnSnS_4−PtM (M = Co, Ni) Nanoheterostructures for
751 Photocatalytic Hydrogen Evolution. *J. Phys. Chem. C* **2015**, *119*,
752 21882−21888.
753 (56) Shavel, A.; Rodríguez-González, B.; Spasova, M.; Farle, M.; Liz-
754 Marzán, L. M. Synthesis and Characterization of Iron/Iron Oxide
755 Core/Shell Nanocubes. *Adv. Funct. Mater.* **2007**, *17*, 3870−3876.
756 (57) Sharma, V. K.; Alipour, A.; Soran-Erdem, Z.; Aykut, Z. G.;
757 Demir, H. V. Highly Monodisperse Low-magnetization Magnetite
758 Nanocubes as Simultaneous T1-T2MRI Contrast Agents. *Nanoscale*
759 **2015**, *7*, 10519−10526.
760 (58) Bediako, D. K.; Lassalle-Kaiser, B.; Surendranath, Y.; Yano, J.;
761 Yachandra, V. K.; Nocera, D. G. Structure−Activity Correlations in a
762 Nickel−Borate Oxygen Evolution Catalyst. *J. Am. Chem. Soc.* **2012**,
763 *134*, 6801−6809.
764 (59) Roger, I.; Symes, M. D. Efficient Electrocatalytic Water
765 Oxidation at Neutral and High pH by Adventitious Nickel at
766 Nanomolar Concentrations. *J. Am. Chem. Soc.* **2015**, *137*, 13980−
767 13988.
768 (60) Chowdhury, D. R.; Spiccia, L.; Amritphale, S. S.; Paul, A.; Singh,
769 A. A Robust Iron Oxyhydroxide Water Oxidation Catalyst Operating
770 under Near Neutral and Alkaline Conditions. *J. Mater. Chem. A* **2016**,
771 *4*, 3655−3660.
772 (61) Dincă, M.; Surendranath, Y.; Nocera, D. G. Nickel-borate
773 Oxygen-evolving Catalyst That Functions under Benign Conditions.
774 *Proc. Natl. Acad. Sci. U. S. A.* **2010**, *107*, 10337−10341.
775 (62) Liu, X.; Jia, H.; Sun, Z.; Chen, H.; Xu, P.; Du, P. Nanostructured
776 Copper Oxide Electrodeposited from Copper(II) Complexes as An
777 Active Catalyst for Electrocatalytic Oxygen Evolution Reaction.
778 *Electrochem. Commun.* **2014**, *46*, 1−4.
779 (63) Singh, A.; Chang, S. L. Y.; Hocking, R. K.; Bach, U.; Spiccia, L.
780 Highly Active Nickel Oxide Water Oxidation Catalysts Deposited from
781 Molecular Complexes. *Energy Environ. Sci.* **2013**, *6*, 579−586.
782 (64) Yu, F.; Li, F.; Zhang, B.; Li, H.; Sun, L. Efficient Electrocatalytic
783 Water Oxidation by a Copper Oxide Thin Film in Borate Buffer. *ACS*
784 *Catal.* **2015**, *5*, 627−630.
785 (65) Zhao, Y.; Vargas-Barbosa, N. M.; Hernandez-Pagan, E. A.;
786 Mallouk, T. E. Anodic Deposition of Colloidal Iridium Oxide Thin
787 Films from Hexahydroxyiridate(IV) Solutions. *Small* **2011**, *7*, 2087−
788 2093.

DOI: 10.1021/acsami.6b09888
ACS Appl. Mater. Interfaces XXXX, XXX, XXX−XXX